In vivo quantitative NMR imaging of fruit tissues during growth using Spoiled Gradient Echo sequence

Samir Kenouche, Marine Perrier, Nadia Bertin, Joulia Larionova, Abderrahmane Ayadi, Michel Zanca, Jérôme Long, Nacer Bezzi, Paul C. Stein, Yannick Guari, et al.

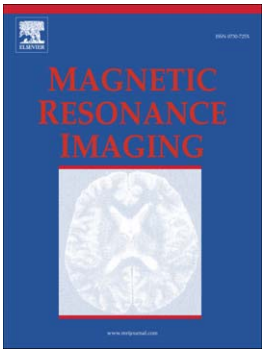

In vivo quantitative NMR imaging of fruit tissues during growth using Spoiled Gradient Echo sequence

S. Kenouche, M. Perrier, N. Bertin, J. Larionova, A. Ayadi, M. Zanca, J. Long, N. Bezzi, P.C. Stein, Y. Guari, M. Cieslak, C. Godin, C. Goze-Bac

PII: S0730-725X(14)00235-5
DOI: doi: 10.1016/j.mri.2014.08.005
Reference: MRI 8228

To appear in: *Magnetic Resonance Imaging*

Received date: 16 July 2013
Revised date: 28 May 2014
Accepted date: 8 August 2014

Please cite this article as: Kenouche S, Perrier M, Bertin N, Larionova J, Ayadi A, Zanca M, Long J, Bezzi N, Stein PC, Guari Y, Cieslak M, Godin C, Goze-Bac C, In vivo quantitative NMR imaging of fruit tissues during growth using Spoiled Gradient Echo sequence, *Magnetic Resonance Imaging* (2014), doi: 10.1016/j.mri.2014.08.005

In vivo quantitative NMR imaging of fruit tissues during growth using Spoiled Gradient Echo sequence

August 14, 2014

S. Kenouche[1] [2]
M. Perrier
N. Bertin J. Larionova A. Ayadi M. Zanca J. Long N. Bezzi P.C. Stein Y. Guari
M. Cieslak C. Godin C. Goze-Bac
Laboratoire Charles Coulomb (L2C) BioNanoNMRI UMR 5221 CNRS, Université Montpellier 2, France
Laboratoire de Technologie des Matériaux et de Génie des Procédés (LTMGP), Faculté des Sciences exactes, Université A. MIRA de Béjaïa, 06000 Béjaïa, Algérie
Institut Charles Gerhardt Montpellier, UMR 5253 CNRS UM2, Chimie Moléculaire et Organisation du Solide, Université Montpellier 2, France
INRA UR 1115 Plantes et Systèmes Horticoles, Domaine Saint-Paul, site Agroparc, 84914 Avignon, 8400 France
Medecine Nucléaire et IRM fonctionnelle, CHU de Montpellier, 34000 France
FKF-SDU, campusvej 55, DK5230 Odense, Danmark
CIRAD/INRIA/INRA, Virtual Plants Team, UMR AGAP, Avenue Agropolis, TA 108/02, 34398 Montpellier Cedex 5, France

Abstract

Non destructive studies of physiological processes in agronomic products require increasingly higher spatial and temporal resolutions. Nuclear Magnetic Resonance (NMR) imaging is a non-invasive technique providing physiological and morphological information on biological tissues. The aim of this study was to design a robust and accurate quantitative measurement method based on NMR imaging combined with contrast agent (CA) for mapping and quantifying water transport in growing cherry tomato fruits. A multiple flip-angle Spoiled Gradient Echo (SGE) imaging sequence was used to evaluate the intrinsic parameters maps M_0 and T_1 of the fruit tissues. Water transport and paths flow were monitored using $Gd^{3+}/[Fe(CN)_6]^{3-}/D-mannitol$ nanoparticles as a tracer. This dynamic study was carried out using a compartmental modeling. The CA was preferentially accumulated in the surrounding tissues of columella and in the seed envelopes. The total quantities and the average volumeflow of water estimated are : 198 *mg*, 1.76 mm^3/h for the columella and 326 *mg*, 2.91 mm^3/h for the seed envelopes. We demonstrate in this paper that the NMR imaging technique coupled with efficient and biocompatible CA in physiological medium has the potential to become a major tool in plant physiology research.

[1] Present address : Place Eugène Bataillon 34095 Montpellier Cedex 5, France. Tel.: +33 6 52 50 44 68
[2] Corresponding author
email: samir.kenouche@univ-montp2.fr

Keywords

Quantitative NMR imaging • intrinsic parameters • compartmental modeling • contrast agents • cherry tomato.

1. Introduction

In plants, the transport and accumulation of water and dry matter in different organs and tissues are major determinants of their growth and final composition [1]. The fluxes of water and carbon exhibit large fluctuations at a short time scale during the diurnal cycle and at a long time scale during the production cycles, depending on plant environment [2]. Current methods to assess these fluxes are either destructive or limited to some organs (e.g. sap flow meters). The fruits are composed of different tissues with a heterogeneous structure and composition. The measurement and mapping of water and other constituents transport is not straightforward, although quite important for understanding fruit growth and final quality in response to internal or external stimuli. The development of methods with high temporal and spatial resolutions which would allow the online *in vivo* monitoring of this information at the tissue or even cell scales is thus a real challenge for the study of these physiological processes and their localization in the fruit. NMR imaging is a non-invasive and non-destructive tool which can provide access to several types of information such as : tissue architecture, spatial and temporal variability of major components like water and sugar and internal flows in fruit during growth. These types of information are more difficult to quantify by conventional destructive methods. Moreover, beyond the simple visualization of morphological structures, quantitatives measurements can be obtained from the NMR images using tissue segmentation and direct evaluation of the signal intensity in the corresponding voxels. During the last two decades this imaging technique has benefited [3,4] to significant theoretical, methodological and intrumental developments . The proton is still the most investigated nucleus because of its abundance and sensitivity in living tissues.

For dynamic studies, fast NMR imaging sequences are a prerequisite for the acquisition of time resolved series of data sets. High temporal resolution gives access to a wide diversity of physiological information. However, it must not sacrifice the signal-to-noise ratio (SNR) quality and the spatial resolution. The T_1, T_2 and M_0 contrasts exist naturally in soft tissues, they take origin from the molecular motions, which are quantified via the spectral density function [5]. These contrasts can be artificially altered by the contrast agent (CA). These paramagnetic substances decrease the T_1 and T_2 of water protons in their surroundings [6]. The CA efficiency is quantified through its longitudinal (r_1) and transversal (r_2) relaxivities.

For *in vivo* studies, there exist a number of physiological constraints affecting the biodistribution of these agents such as the size, the shape, their hydrophilic and hydrophobic character and especially the chemical nature of coating-ligands [7]. The grafting of biocompatible functional molecules will enable one to combine their intrinsic properties to those of the nanoparticles. In this study, the ultrasmall nanoparticles of $Gd^{3+}/[Fe(CN)_6]^{3-}$ stabilized by *D-mannitol* have been used as T_1-relaxing CA. They present an interest for *in vivo* plant tissues investigations because : (1) they provide a r_1 value four times higher over commercial CA (such as ProHance®) (2) they are water soluble, not aggregated (3) they provide a stable aqueous physiological colloidal solution (4) they present an ultrasmall size of 3.4 *nm* that permit their circulation in the plant. Fast and accurate T_1 and M_0 mapping approach to study plant tissues was implemented on a voxel-by-voxel basis using multiple

flip-angle Spoiled Gradient Echo (SGE) acquisition. The T_1 values for each voxel are calculated from the ratio of signal intensities, based on the assumption of a simple exponential recovery. The accuracy of the variable flip-angle technique is evaluated in phantom before being applied *in vivo*. The choice of flip angles can significantly affect the precision of the derived T_1 values. Indeed, we developed an algorithm in order to find the optimal combination of flip angles to achieve optimal T_1 mapping accuracy. To correct for inhomogeneous B_1 excitation, a B_1 map was determined using the Double Angle Method [8] . An efficient error mapping procedure to assess the uncertainties associated with each voxel of the quantitative images is presented. An accurate and robust segmentation procedure, based on the calculation of the maximum of the derivative after Gaussian smoothing of NMRimages, was developed in order to localize the tissues where a signal enhancement was detected. Based on this segmentation, the physiological features of the immature-green cherry tomato were investigated from the kinetic study of the CA used as tracerof water transport in the fruit during growth. This kinetic study was carried out using compartmental modeling. Several research works on molecular transport have been carried out at the stem and root plants levels [9,10]. To our knowledge, few publications have been devoted to investigate the water transport and ditribution within the fruit [11,12,13]. The purpose of the present study was the implementation of a methodology for quantitative measurements using NMR imaging combinedwith efficient and biocompatible CA dedicated to study the physiological changes related to water movement within the fruit.

2. Materials and methods

2.1. CA

In this section we briefly present the synthesis and characterizations of $Gd^{3+}/[Fe(CN)_6]^{3-}/D-mannitol$ nanoparticles used as CA. The auto-assembling reaction between $Gd(NO_3)_3$ and $K_3[Fe(CN)_6]$ in water in the presence of tD-mannitol (see Fig. 1S, Electronic Supporting Information (ESI)) yields to aqueous solution of nanoparticles $Gd^{3+}/[Fe(CN)_6]^{3-}/D-mannitol$. Infrared spectra were recorded as KBr disks on a Perkin-Elmer 1600 spectrometer with a $4\,cm^{-1}$ resolution. Elemental analyses were performed by the Service Central d'Analyses (CNRS, Vernaison, France). The samples were heated at 3000 C° under He. Oxygen was transformed in CO and detected by using an IR detector. Metals were determined with a high resolution ICP-MS using a ThermoFischer element. Transmission Electron Microscopy (TEM) observations were carried out at 100 kV (JEOL 1200 EXII). Samples for TEM measurements were deposited from solutions on copper grids. The nanoparticles size distribution histogram were determined using enlarged TEM micrographs taken at magnification of 100 K on a statistical sample of 300 nanoparticles. The T_1 and T_2 relaxation times of hydrogen protons in aqueous solutions at various concentrations of nanoparticles were performed on a Tecmag Apollo spectrometer operating at $200\,MHz$. T_1 values were obtained from inversion recovery sequence (180° - τ - 90°) with the following parameters: $T_R = 8\,s$, 4 averages and 90° pulse delay $= 132\,\mu s$. For each concentration of the CA, the inversion times (τ) were chosen such that the instantaneous magnetization recovers its equilibrium value. The Carr-Purcell Meiboom Gill pulse sequence (90°-$(180^{\circ})_n$-) was applied to achieve the T_2 measurement. The sequence parameters were as follows: 90° - 180° pulse spacing was $3.2\,ms$, $T_R = 5\,s$, 8 averages and 90° pulse delay

$=132\,us$. For each concentration of CA, the number of echos (*n*) is selected to allow a complete decay of the transverse magnetization. The r_1 and r_2 relaxivities were then calculated from the slope of a linear regression of $R_{1,2}=T_{1,2}^{-1}$ versus CA concentration (*C*) : $R_{1,2}=R_{1,2}^0+r_{1,2}\times C$. The $R_{1,2}^0$ are the relaxation rates without CA.

2.2. B_1 *inhomogeneities correction*

For in vivo NMR imaging at high field (≥ 3 Tesla) it is essential to consider the homogeneity of the B_1 field, especially for T_1 quantification. This inhomogeneity may arises from different sources, like amplifier non-linearity in thelow output region, intrinsically low SNR, and tissue dielectric effects. B_1 inhomogeneity lead to significant spatial variations in the image contrast and intensity, making quantitative image interpretation and segmentation difficult to achieve. In this paper, the correction for the B_1 inhomogeneities was carried out by division of pixels of tomato images by the corresponding pixels of the water phantom image. We evaluated the B_1 inhomogeneities using the Double Angle Method [8]. Such methods allow calculation of a flip-angle map, which is an indirect measure of the B_1 field. Two images were acquired: I_1 with prescribed angle $\alpha=30^\circ$ and I_2 with prescribed angle $\alpha_2=2\alpha$ (see Fig. 2S, ESI). All other sequence parameters are kept constant: $T_R=10\,s$ and $T_E=6\,ms$. Flip angles map was calculated according to the formula : $\alpha=\arccos(I_2/2I_1)$.

2.3. θ_1 *and* θ_2 *optimization*

The simulation was implemented using an in-house developed program written using MATLAB (The MathWorks, Natick, MA) software. This algorithm was developed in order to find the optimal combination of flip angles that minimize the error in T_1. The error in T_1 being estimated from the residue between the T_1 measured by NMR relaxometry using an inversion-recovery pulse sequence (the reference T_1 values) and T_1 values computed from multiple flip-angle acquisitions using SGE sequence from the phantom. Simulation was performed using five test tubes filled with aqueous solutions at various CA concentrations (10^{-3}, 2.5×10^{-4}, 10^{-4}, 8.5×10^{-5} and 10^{-5} (mol/L)), producing wide range of T_1 values from 240 to $1300\,ms$. Phantom data were acquired with the following parameters : $\alpha_1=12^\circ$, $\alpha_2=56^\circ$, $T_E=6\,ms$, 64 averages and $T_R=110\,ms$ resulting in a total acquisition time of $30\,min$.The simulation was conducted for two ranges of flip angles from 6° to 21° and from 36° to 60°. Optimum flip angles were calculated to be 8° and 60° (see Figs. 3S and 4S, ESI).

2.4. Set-up monitoring contrast agent uptake

In this experiment, the dynamic transport of water in immature-green tomato was investigated using $Gd^{3+}/[Fe(CN)_6]^{3-}/D-mannitol$ as a tracer. Cherry tomato (Solanum lycopersicum) grown under glasshouses at INRA (Institut National de la recherche Agronomique, Avignon France) was used in this study. Rapidly growing fruits, about 15 days old (from anthesis), were removed from the plant and placed under sterile conditions in glass tubes filled with a nutrient

solution ($4.4\,gL^{-1}$ of Murashige and Skoog medium (MS 5519, Sigma-Aldrich, Sa int Louis, MO) and $60\,gL^{-1}$ of sucrose), in which the fruit pedicel was immersed [14]. The CA was added at a concentration of 10 $mmol/L$ in the nutrient solution in order to be taken up by the fruit. The fruit pedicel was kept in the nutrition medium throughout the experiments. The total height of the fruit and pedicel was about 4.4 *cm* (3 *cm* for the pedicel and 1.4 *cm* for the fruit). A bird-cage radio frequency (RF) coil with 3 *cm* inner diameter, wrapped around the tube containing the fruit, transmits the excitation pulses and receives the NMR signal. Sinc-function pulse (2 *ms*) was applied for selective excitation. The whole setup (Fig. 1) was loaded in a 4.7 T magnet of an NMR spectrometer operating at a proton frequency of 200 *MHz* and then investigated for five days duration using a SGE pulse sequence. The temperature conditions in the magnet were $21 \pm 1\ ^{\circ}C$ during the day and $19 \pm 1\ ^{\circ}C$ during the night. Using the implemented SGE sequence, five transversal slices were acquired at different fruit offsets. After frequency-distance conversion the offsets were : 1.1, 4.3, 7.5, 10.7 and 13.9 *mm* with respect to lowest part of the fruit. Slices were acquired in a sequential mode, in ascending order. For each offset we performed a T_1-weightedimage followed by another M_0 -weighted one. We recorded sixty images for each slice (thirty T_1-weighted and thirty M_0 -weighted), which means a total of three hundred (5 slices $\times$ 2 weighting $\times$ 30 acquisition for each weighting) images obtained during five days of acquisition. The sequence parameters were as follows: $T_E = 6\,ms$, optimized flip angles ($\theta_1 = 8^{\circ}$ and $\theta_2 = 60^{\circ}$), spatial resolution = $100\,\mu m \times 100\,\mu m$, slice thickness = $750\,\mu m$, field of view (FOV) = 25^2 mm^2 , slice gap $= 3.2\,mm$, matrix size = 256^2 (512^2 after zero filling) and $T_R = 110$ *ms* resulting in a total acquisition time of 24 *min* .

The kinetic study was conducted on the segmented tissues. The changes in tracer concentration in the columella are described by transports between compartments which represent separate regions. The rate of transfert from one compartment to another is proportional to the concentration in the compartment of origine and to a rate constant (k_1 , k_{m1}, k_{12} , k_{23} and k_{34} (h^{-1})). k_1 was assigned to the precipitation of nanoparticles in the pot. As illustrated in Fig. 2, each compartment is associated with a slice. The first compartment is the nutrient medium (the pot) from which the tracer progresses to the following compartments. *m(t)*, represents the CA concentration in the pot. Tobe rigorous the meaning of the concentration and the kinetic rates must be understood as 'equivalent concentration' and 'equivalent rates' respectively.

2.5. T_1 and M_0 mapping

The quantitative analysis presented in this section was achieved by applying a series of processing steps using MATLAB software. At the beginning, the raw data acquired from the MRI scanner (Apollo, Tecmag), were processed through the following mathematical operations : baseline correction, apodization, zero filling and 2D Fourier transform, respectively. All these operations aim to improve the image quality in order to perform post-treatment under better conditions. All raw data have undergone the same mathematical processing. Once the images are constructed, T_1 maps were calculated using Eq. (2) from two NMR images acquired from the optimized flip angles $\theta_1 = 8^{\circ}$ for M_0-weighted (S_1) and $\theta_2 = 60^{\circ}$ for T_1-weighted (S_2). Subsequently, T_1 maps were converted into CA concentration maps using Eq. (5) on a voxel-by-voxel basis. According to the theoretical equation for SGE signal intensity, the signals ratio corresponding to θ_1 and θ_2 flip angles is given by :

$$\frac{S_2}{S_1} = \frac{1-e^{(-T_R/T_1)}\cos\theta_1}{1-e^{(-T_R/T_1)}\cos\theta_2} \times \frac{\sin\theta_2}{\sin\theta_1} \quad (1)$$

The T_1 maps have been computed on a voxel-by-voxel basis :

$$T_1 = \frac{-T_R}{\log\left(\frac{S_1\sin\theta_2 - S_2\sin\theta_1}{S_1\cos\theta_1\sin\theta_2 - S_2\cos\theta_2\sin\theta_1}\right)} \quad (2)$$

Eq. (2) has been solved considering the following constraint :

$$0 < \frac{S_1\sin\theta_2 - S_2\sin\theta_1}{S_1\cos\theta_1\sin\theta_2 - S_2\cos\theta_2\sin\theta_1} < 1 \quad (3)$$

This constraint ensures reliable and reasonable measurement of T_1 by excluding the outliers, such as the negative and complex values. Once the T_1 has been calculated, the proton density maps were obtained from the theoretical equation for SGE signal intensity :

$$M_0 = S_2 \times \frac{1-e^{(-T_R/T_1)}\cos\theta_2}{\left(1-e^{(-T_R/T_1)}\right)\sin\theta_2} \quad (4)$$

M_0 maps were calculated according to S_2 images since the SNR ratio is better compared to S_1 images. Finally, we derived an analytical formula to transform longitudinal relaxation time T_1 change to CA concentration change using varied $T_{1,0}$ and the linear relationship between $R_1 = 1/T_1$ and CA concentration, according to :

$$C(t) = \frac{1}{r_1}\sum_{i=1}^{n}\left(\frac{1}{T_1^i(t)} - \frac{1}{T_{1,0}^i(t)}\right) \quad (5)$$

Where $T_{1,0}$ is the relaxation time without CA.

2.6. Errors computing

The accuracy and precision of calculation methods depend on the magnitude of systematic and random errors. Various error sources in NMR imaging experiments lead to deterioration of the image quality and can actually distort all calculations and thus the interpretation of results. The noise may be generated within the receiver coil and other electronics [15].

It is clear that the voxels exhibiting the lowest signal intensity (tissues with low proton density and/or long T_1) will be most affected. Consequently, it is necessary to use a robust method (without approximations) to quantify and minimize these errors as far as possible. The assessment of the uncertainty committed in each pixel on the parametric images was conducted by computing the total differential of T_1 and M_0. The relative error on T_1 maps can be written as :

$$\frac{\Delta T_1}{T_1} = |\Psi_1|\frac{\Delta S_1}{S_1} + |\Psi_2|\frac{\Delta S_2}{S_2} \quad (6)$$

We search :

$$\Psi_1 = \frac{\partial T_1}{\partial S_1}\frac{S_1}{T_1}, \quad \Psi_2 = \frac{\partial T_1}{\partial S_2}\frac{S_2}{T_1} \tag{7}$$

The same calculation method is applied to estimate the relative error for M_0 maps, according to :

$$\frac{\Delta M_0}{M_0} = \left|\frac{\partial M_0}{\partial S_2}\frac{S_2}{M_0}\right|\frac{\Delta S_2}{S_2} + \left|\frac{\partial M_0}{\partial T_1}\frac{T_1}{M_0}\right|\frac{\Delta T_1}{T_1} \tag{8}$$

The noise variances (ΔS_1 and ΔS_2) were evaluated from the maximum of the probability density function (PDF) of background pixels intensities (magnitude images), which are described by Rayleigh distribution [16]. All the pixels with a relative error exceeding 15 % in the computed images were eliminated and hence were not included in extracting the physiological and morphological information.

2.7. Phantom imaging

Before proceeding with the fruit imaging study, the Eq. (2) was tested on a phantom in order to test its reliability. The phantom (Fig. 3) used is the same as that presented in section 2.3. The CA concentration increases in ascending order from tube 1 to tube 5. The experimental parameters for these experiments were: FOV = 25 $mm, slicethickness = 750$ μm, optimized flip angles $= 8^\circ$ and 60°, $T_E = 6\,ms$, $T_R = 110\,ms$ and 64 averages resulting in a total acquisition time of 30 min. The basic idea for this analysis was to compare the T_1 measured by NMR relaxometry using an inversion-recovery pulse sequence (the reference T_1 values) and T_1 values computed from multiple flip-angle acquisitions using SGE imaging sequence.

3. Results and discussion

3.1. CA characterization

The Gd/Fe ratio obtained from elemental analysis is equal to c.a. 1.04, similar the value of 1 expected for the bulk analogous $Gd(H_2O)4[Fe(CN)_6]$. InfraRed spectroscopy (shift of the cyanide stretching vibrations toward higher frequencies in comparison with the hexacyanoferrate precursor) as well as *X-Ray* diffraction (orthorhombic system with a Cmcm space group, Fig. 5S, ESI) confirms the formation of the cyano-bridged network. Transmission Electronic Microscopy measurements (Fig. 6S, ESI) show that the nanoparticles are spherical in shape with no sign of aggregation. The T_1 and T_2 relaxation time measurements performed for aqueous solutions of the nanoparticles at various concentrations give the longitudinal and transverse relaxivities equal to 11.4 ±0.1 and 12.6 ±0.1 $mM^{-1}s^{-1}$, respectively. The r_2/r_1 ratio equal to 1.10. These values are four times larger than the ones obtained for commercial ProHance® (3.00 pm 0.01 *and* 3.41 ±0.01 $mM^{-1}s^{-1}$ for r_1 and r_2 at 4.7 *T*, respectively). These measurements confirm that the nanoparticles may be used as efficient T_1-relaxing CA.

3.2. Method validation

The contrast between the different tubes in the image acquired at 8° flip angle was caused by a residual T_2^* weighting. As demonstrated in Fig. 4, the T_1 calculated using the variable flip-angle technique are ingood agreement with the T_1 measured by NMR relaxometry using an inversion-recovery pulse sequence. The highest error (about 20%) was observed for the longest T_1. This is explained by the low SNR recorded for this tube, because it knowsthat a slight decrease in this ratio affects many more long T_1 than short T_1. However, this T_1 value is not included in the range of T_1 affected by the CA, (seen Fig. 7S, ESI).

3.3. MRI of tomato fruit

As illustrated in Fig. 5, the main anatomic features (pericarp, seeds, placental tissue, seed envelopes, columella and locular tissue) composing cherry tomato are clearly identified. The images presented are those of slice 2 (see Fig. 1). The results of the corresponding T_1, M_0, $\Delta T_1 / T_1$ and $\Delta M_0 / M_0$ maps are shown in Fig. 6. In view of these results, T_1 and M_0 images enabled a good discrimination of the morphological and structural tissue characteristics. The images 6b, 6e show the maps of the relative errors $\Delta M_0 / M_0$, $\Delta T_1 / T_1$ calculated in the selected slice using Eq. (8) and (6), respectively. Both relative errors are consistently higher in radial walls of the pericarp, columella and placental tissue than in other tissues, indicating that both M_0 and T_1 are overestimated in these structures. The highest errors were then observed for the tissues characterized by long T_1 values and low proton densities (low M_0 value). These findings certainly reflect the low SNR derived from T_1– and M_0-weighted images, recorded in these rigidified tissues. Therefore, it is unrealistic to calculate T_1 and M_0 maps in these regions, as can be seen in the images 6a, 6d, 6g and 6j. Indeed, T_1 and M_0 maps were corrected by retaining only the pixels exhibitinga relative error not exceeding a statistical threshold based on a 15 $\%$ acceptance criterion. The set of pixels in these regions were thus removed (black pixels), as can be seen on the images 6c and 6f. These images were obtained by applying the masks 6b and 6e on the images 6a and 6d, respectively. We have observed that these relative errors decrease progressively in proportion to the quantity of CA and water molecules were taken up by the fruit, as shown in the images 6h and 6k. This error decrease is thus explained by the signal enhancement recorded in these tissues. We mainly attribute this oversignal intensity to decrease of the longitudinal relaxation times of tissue protons by paramagnetic interactions with CA. This signal intensity enhancement is also attributed to the increase of the proton density during the fruit growing. These observations are clearly highlighted by the weighted images. As mentioned previously, the voxels exceeding an error of 15 $\%$ were eliminated (black pixels), see the images 6i and 6l. These images were obtained by applying the masks 6h and 6k on the images 6g and 6j, respectively.

It was discussed in several studies [17,18], that free water is the key area where biological reactions take place, consequently, the mobility degree of water molecules in the cell is considered to control the physiological activities in the living tissues. In addition, water is the major biological constituent, providing the liquid support and solvent environment for most biochemical reactions [19,20]. In this work, we checked that the T_2^* relaxation effect did not significantly attenuated the proton density images (data not shown). From the images 6c,

we observe a high signal intensity in the pericarp, in the locular tissue and to a lesser extent in the seed envelopes. In pericarp, an increasing gradient of signal was observed from the inner to the outer paricarp. In contrast, low proton density is observed in the columella and radial wall of the pericarp. The lowest proton density was detected in the seeds. Within the same tissue, we found heterogeneous distributions of T_1 and M_0. This reflects the presence of both free and bound water molecules. The cell density and diversity of sizes and shapes of the cells making up these tissues may also contribute to this heterogeneity [21]. For instance, small homogeneous cells are located at the inner (near the locules) and outer (near the epidermis) pericarp while the mesocarp is made of big heteregeneous cells [22]. The columella is a parenchymatous tissue withlarge cells and air spaces. According to the images 6c and 6f, we see a correlation between the M_0 and T_1 values in both the pericarp and seed envelopes. The more the tissue is rich in free water, the longer isits T_1. This proportionality is partially observed in locular tissue. The images 6i and 6l reflect the proton density and T_1 distributions at the end of the experiment. A significant increase of the water density is observed in the seed envelopes, columella and spreaded in all area around this vascular bundles, during fruit development. This wide enlargement of the bright area in the surrounding tissues of columella can be explained by the existence of a radialtransport. It is interpreted in terms of molecular diffusion and permeation (depending on the selective permeability of membranes) inside and accross cells in the plant tissues [10]. In addition, it has been demonstrated that this broadening is proportional to the magnitude of molecular diffusion and permeation. Surprisingly, a very slight signal enhancement was recorded in the pericarp. These results suggest that under these conditions, water and CA preferentially moves through the central vascular bundles of the fruit (perhaps of bigger size) and not in vessels at the fruit periphery. The signal enhancement in seed envelopes confirmed that they are active sinks at this period of fruit development mainly supplied by branches of the inner vasculature. It should be noted that, at the end of the experiment, the fruit had grown by $15\ \%$ compared to its initial volume (as outlined below).

3.4. Segmentation

It is important to establish a robust procedure to discriminate unaffected and enhanced signal intensity regions. Segmentation operation was carried out by computing the maximum of the derivative after Gaussian smoothing of the NMR images. As shown inFig. 7, each color in the segmented images represent a set of pixels having the same evolution of signal intensity during the experiment. The blue color reflects the tissues where no significant signal enhancement effect was observed. The red and yellow colors reflect the tissues where a significant signal enhancement effect was detected. The red pixels volumes in each slice are: 4.45, 11.30, 1.55, 0.82 and $0\,mm^3$, respectively. The yellow pixels volumes in each slice are: 0, 14.90, 10.70, 11.35 and $0\,mm^3$, respectively. The seed envelopes, columella and its surrounding tissues are clearly identified. The seed envelopes were not observed for the slices 1 and 5. As can be seen in the schematic illustration of the NMR imaging setup, these slices are located at the bottom and at the top of the tomato fruit. No signal enhancement was revealed in the slice 5, suggesting that no water containing tracer reached this part of the fruit in the total time of experiment.

The CA distribution within the fruit was tissue dependent, but it was uniform for a given tissue. Change in the images affected by CA (superimposing of the CA concentration map on the anatomical image, Fig. 8) indicates that cell activity is higher in seed envelopes, columella and its surrounding tissues. The biodistribution of tracer in the fruit may have occurred by mass

flow or by active transport which are of similar importance at this stage of fruit development [23].This experiment proved that functionalized CA are small enough to move in the conducting vessels and through the phloem sieve plat pores, in accordance with experimental observations of pore diameters which are around $0.5\ \mu m$ [14]. The $T_{1,0}$ varies from about 10% (see Fig. 8S, ESI) during the experiment. Indeed, when calculating CA concentration in the tissues, we took into account $T_{1,0}$ change from $950\,ms$ to $1100\,ms$ in the columella and from $850\,ms$ to $1090\,ms$ in the seed envelopes (see Eq. (5)).

3.5. CA kinetic analysis for the segmented tissues

Behaviour of the CA concentration versus time curves may be explained by three phases of the data acquisition. Starting from baseline, no absorption was observed, the plant tissues uptake the tracer and their concentration increases. It systematically increases up to a certain level and then exhibits a plateau of variable width. These features were observed for each slice. Another important parameter to characterize this dynamic behaviour is the time of onset enhancement (t_0 , is the time point where the contrast agent reaches the NMR image plane). All the parameters (rate constant and time of onset enhancement) of this compartmental modeling were obtained by Levenberg-Marquardt nonlinear fitting Algorithm. In order to ensure a better accuracy of the fitting parameters, we repeated the fitting procedure for several choices of initial values for each parameter. Only the solution that minimized the chi-square error χ^2 was retained. The various adjustment parameters obtained from this modeling are listed in the following table :

From these kinetic parameters, we have a 2 hours increment between slices. Furthermore, the amount of CA decreases with distance from the pedicel. The rate constants also decreased along a similar trend.

As shown in Fig. 9, in the columella the signal enhancement appears after about 58 *h* of data acquisition. In Fig. 10, the fruit uptakes water and its volume increased regulary whith a segmoidal curve. In Figs. 11 and 12, in the seed envelopes the signal enhancement effect was visible from the first images and the tracer appeared at the beginning of the experiment. In addition, the concentration increases linearly withtime. The late onset recorded in the columella can be explained by the following assumptions : (1) the seed envelopes are the place of accumulation of CA while the columella is a place of their passageway (conducting vessels). Therefore the CA are better visibile where they accumulate.

(2) based on the growth curve, at about $t = 59\ h$ volume flux increases which could result to a large amount of CA in the columella and possibly a saturation effect in the seed envelopes.

(3) it was reported [24] a significant presence of air bubbles in the columella. These air bubbles creating large local field anisotropies affecting the NMR signal, no signal enhancement was observed during the first hours. However, the signal enhancement appears when the flow is maximum (this flow corresponds to inflexion point of the growth curve). These hypotheses need to be confirmed by further experiments. As stated above in the seed envelopes T_1 changes are not following water uptake. Our findings indicate that the observed T_1 decrease in this tissue is not related to a physiological effect (changes in the structural aspects of tissues) but it could be caused by the presence of the CA. We have confirmed this result through the study on a control tomato. For this fruit without CA, we found a positive correlation (see Fig. 8S, ESI) between changes in T_1 and M_0 . The T_1 variation was discontinuous, from progressive and regular at the beginning (related to the increasing load of free water), to constant for some time after (probably this is due to the binding of free water to organic molecules). T_1 changes are also related to the transpiration cycles (active and slow

transpiration) of the fruit ite25. This positive correlation is a typical characteristic of a purely physiological effect [6].

The total amount of water accumulated in the fruit over the experiment was evaluated from all slices by an extrapolation to a spherical volume. From this computation a quantity of 310 *mg* was found which represents the net influx (import of water minus loss of water by transpiration). In a second time and in order to quantify the total quantity of tracer uptake by the fruit throughout the experiment, we built a model based on trapezoidal volumes. This model was constructed as follows : knowing the total amounts of CA in the slices 1, 2, 3 and 4, the intermediate quantities (between slices) have been assessed by considering a trapezoidal volume. The bases of the trapezoids are the surfaces of each segmented tissues and the height is equal to the slice thickness. The same computational procedure was used to evaluate the total volume in the seed envelopes and in the columella. On the basis of this approach, the total quantities of CA obtained both in the columella and in the seed envelopes were : 18.65 and 30.58 μg, respectively. These amounts correspond to the volumes : 59.86 mm^3 for the columella and 98.72 mm^3 for the seed envelopes. At the end of the experiment, the CA quantity contained in 15 *g* of water corresponds to 1.4 *mg*. Thus, from the estimated total amount of the tracer in the fruit, we can predict the total water quantity uptake using this proportionality relationship. The total quantities and the average volume flow of water estimated are : 198 *mg*, 1.76 mm^3/h for the columella and 326 *mg*, 2.91 mm^3/h for the seed envelopes. The total amount of water uptake by the fruit was 524 *mg* duringthe whole experiment. The fruit transpiration was estimated based on fruit conductance measured on detached fruits from the same cultivar grown under similar conditions (data not shown). We could estimate a loss of water of about 100 to 150 *mg* over 5 days depending on air humidity. So the uptake of water, which is the sum of net accumulation and transpiration, is in good agreement with the amount estimated from the growing curve, confirming that $Gd^{3+}/[Fe(CN)_6]^{3-}/D-mannitol$ canbe efficiently used to track water within the fruit.

4. Conclusion

In this paper, the total amount of water uptake has been investigated by analysing the progress of tracer in cherry tomatoes using quantitative NMR imaging measurements. The results reported in this work emphasize that SGE sequence combined with efficient and biocompatible CA offer the possibility to quantitatively assess and monitor dynamic processes in fruits. We chose to reach an artificial positive contrast (T_1 effect) instead of negative contrast (T_2 effect) for image acquisition. The negative contrast can be easily mistaken with the hyposignal caused by local field inhomogeneities, magnetic susceptibility artifacts and inherent noise of the NMR imaging experiments. Water transport and content are major factors controlling the plant morphology and development. It has been shown that the knowledge of T_1 and M_0 distributions is useful for the characterization of the physical state of the water in biological tissues than a simple visual interpretation of weighted images. This water mobility is directly related to physiological activity and its understanding is of fundamental relevance in the plant physiology studies. The current in vivo results clearly demonstrate that CA distribution within the fruit is tissue dependent and almost homogeneous for a given tissue. Indeed, this tracer was preferentially accumulated in seed envelopes and tissues surrounding the columella. From this finding and at this stage of fruit development, we have emphasized that these tissues are active sinks in growing fruits. The knowledge of the vascular network distribution is paramount to understand the transport pathways in the fruit. These investigations open new perspectives to use these type of CA in agricultural systems for more systematic studies. Work is in progress in

order to studythe process of biodistribution of the CA coated with glucose or fructose. These sugars are the major elements responsible for tissue growth. Moreover, performing 3D acquisitions instead of 2D acquisitions reduces the imperfection effects of pulses selection and allows a better assessment of fruit growth.

Appendix A

The equivalent rates k_i (h^{-1}) are assumed to be linearly related to the difference of equivalent concentration of CA between two compartments. Differential equations that describe the kinetic behavior of CA in the tissues are given by:

$$\begin{cases} \dfrac{dm(t)}{dt} = -(k_1 + k_{m1}) \times m(t) \\ \dfrac{dc_1(t)}{dt} = k_{m1} \times m(t) - k_{12} \times c_1(t) \\ \dfrac{dc_2(t)}{dt} = k_{12} \times c_1(t) - k_{23} \times c_2(t) \\ \dfrac{dc_3(t)}{dt} = k_{23} \times c_2(t) - k_{34} \times c_3(t) \\ \dfrac{dc_4(t)}{dt} = k_{34} \times c_3(t) \end{cases} \quad A1(9)$$

Where *m(t)*, [EQUATION], $c_2(t)$, $c_3(t)$ and $c_4(t)$ are defined as a kind of equivalent concentrations of CA at time *t* for each compartment. The initial equivalent concentration of the CA in each slice is null $c_i(0) = 0$, we get the following formulas to estimate the kinetic parameters:

$$\begin{cases} {}_1(t) = k_{m1} \times \int_0^t m(u) e^{-k_{12}(t-u)} du \\ \text{c}\, c_2(t) = k_{12} \times \int_0^t c_1(v) e^{-k_{23}(t-v)} dv \\ c_3(t) = k_{23} \times \int_0^t c_2(w) e^{-k_{34}(t-w)} dw \end{cases} \quad A2(10)$$

These integrals have been numerically solved. The onset times (t_0) were obtained according to the following formula:

$$c_i(t) = \begin{cases} c_i(t - t_0) & \Rightarrow \quad t \geq t_0 \\ 0 & \Rightarrow \quad t < t_0 \end{cases} \quad A3 \qquad (11)$$

Appendix B. Supplementary material

The following materials are available in the online version of this article.

Supplemental Sch. S1. Representation of *D-mannitol* used as stabilising agents.

Supplemental Fig. S2. Flip angles mapping.

Supplemental Fig. S3. θ_1 optimal flip angle minimizing the error in T_1.

Supplemental Fig. S4. θ_2 optimal flip angle minimizing the error in T_1.

Supplemental Fig. S5. X-Ray diffraction pattern for $Gd^{3+}/[Fe(CN)_6]^{3-}/D-mannitol$ nanoparticles.

Supplemental Fig. S6. Transmission Electronic Microscopy image of $Gd^{3+}/[Fe(CN)_6]^{3-}/D-mannitol$ and their size distribution histogram.

Supplemental Fig. S7. T_1 changes in the columella in the fruit with CA.

Supplemental Fig. S8. T_1 and M_0 changes in the control tomato (without CA).

References

[1] Guichard S, Gary C, Leonardi C, Bertin N. Analysis of Growth and Water Relation of Tomato Fruits in Relation to Air Vapor Pressure Deficit and Plant Fruit Load. Journal of Plant Growth Regulation 2005;24:1-13.

[2] Van As H, Scheenen T, Vergeldt FJ. MRI of intact plants. Photosynth Res. 2009;102:213-222.

[3] Chudek JA, Hunter G. Magnetic resonance imaging of plants. Progress in Nuclear Magnetic Resonance Spectroscopy 1997;31:43-62.

[4] Borisjuk L, Rolletschek H, Neuberger T. Surveying the plant's world by magnetic resonance imaging. The Plant Journal 2012;70:129-146.

[5] Xia Y. Contrast in NMR imaging and microscopy. Concepts in Magnetic Resonance 1996;8:205-225.

[6] Callaghan PT. Principles of Nuclear Magnetic Resonance Microscopy. Oxford: Oxford University Press; 1993.

[7] Bin na BH, In Chan S, Hyeon T. Inorganic nanoparticles for MRI contrast agents. Adv. Mater. 2009;21:2133-2148.

[8] Cunningham C, Pauly J, Nayak K. Saturated Double-angle Method for Rapid *B-1* Mapping. Magnetic Resonance in Medicine 2006;55:1326-1333.

[9] Scheenen TWH, Vergeldt AM, Heemskerk AM, Van As H. Intact plant Magnetic Resonance Imaging to Study Dynamic in Long-Distance Sap Flow Conducting Surface Area. American Society of Plant Biologists 2007;144:1157-1165.

[10] Gussoni M, Greco F, Vezzoli A, Osuga T, Zetta L. Magnetic resonance imaging of molecular transport in living morning glory stems. Magnetic Resonance Imaging 2001;19:1311-1322.

[11] Kuchenbrod E, Kahler E, Thurmer F, Deichmann R, Zimmermann U, Haase A. Functional magnetic resonaance imaging in intact plants-quantitative observation of flow in plant vessels. Magnetic Resonance Imaging 1998;3:331-338.

[12] Rokitta M, Zimmermann U, Haase A. Fast NMR Flow Measurements in Plants Using FLASH Imaging. Journal of Magnetic Resonance 1999;137:29-32.

[13] Van As H. Intact plant MRI for the study of cell water relations, membrane permeability, cell- to-cell and long distance water transport. J. Exp. Bot. 2007;58:743-756.

[14] Bussières P, Bertin N, Morris CE, Vigne C, Orlondo P, Glaux C, Floret H, Bernadac J, Sévénier V, Korownikkof S. High external sucrose concentration inhibits the expansion of detached tomato fruits grown in a novel semi-open device. In Vitro Cellular and Developmental Biology - Plant 2011;47:743-751.

[15] Hoult DI, Richards RE. The Signal-to-Noise Ratio of the Nuclear Magnetic Resonance Experiment. Journal of Magnetic Resonance 1976;24:71-85.

[16] Bonny JM, Renou JP, Zanca M. Optimal Measurement of Magnitude and Phase from MR Data. Journal of Magnetic Resonance 1996;113:136-44.

[17] Zlatev Z, Lidon FC. An overview on drought induced changes in plant growth, water relations and photosynthesis. Emir. J. Food Agric. 2012;24:57-72.

[18] Maurel C, Chrispeels MJ. Aquaporins. A Molecular Entry into Plant Water Relations, American Society of Plant Physiologists 2001;125:135-138.

[19] Ortega JKE. Plant Cell Growth in Tissue. American Society of Plant Physiologists 2010;145:1244-1253.

[20] Kenouche S, Larionova J, Bezzi N, Guari Y, Bertin N, Zanca M, Lartigue L, Cieslak M, Godin C, Morrot G, Goze-Bac C. NMR investigation of functionalized magnetic nanoparticles *Fe-3O-4* as T_1 - T_2 contrast agents. Powder Technology 2014;255:60-65.

[21] Kuchenbrod E, Haase A, Benkert R, Schneider H, Zimmermann U. Quantification NMR Microscopy on Intact Plants. Magnetic Resonance Imaging 1995;13:447-455.

[22] Wang F, Sanz A, Brenner ML, Smith A. Sucrose Synthase, Starch Accumulation, and Tomato Fruit Sink Strength. Plant Physiol. 1993;101:321-327.

[23] Liu G, Wang X, Yang Q, Wei M. Advances in studies on chemical constituents and pharmacological actions of *Cordyceps sinensis*. Food Sci. Technol. 2007;32:202-209.

[24] Musse M, Quellec S, Devaux MF, Cambert M, Lahaye M, Mariette F. An investigation of the structural aspects of the tomato fruit by means of quantitative nuclear magnetic resonance imaging. Magnetic Resonance Imaging 2009;27:709-719.

[25] Johnson GA, Brown J, Kramer PJ. Magnetic resonance microscopy of changes in water content in stems of transpiring plants. Proc. Natl. Acad. Sci USA 1987;84:2752-2755.

Table 1. Kinetic analysis for the columella

index	k_{index} (h^{-1})	t_0 (h)
1	0.020	/
m1	0.014	58.25
12	0.710	60.90
23	0.506	63.40
34	0.211	/

Figure 1. **Schematic illustration of the NMR imaging setup. The RF coil assembly was disposed around the fruit.** T_x **and** R_x **symbolize the RF transmission and reception of the NMR signal, respectively.**

Figure 2. **Kinetic study in the columella using a compartmental modeling.**

Figure 3. **Normalized SGE images for the phantom. The images were acquired from 8° (a) and 60° (b) flip angles. Each number appearing on the image is associated to a concentration of CA.**

Figure 4. **Comparison of the T_1 values measured by NMR relaxometry (reference T_1) and imaging (Eq. (2)) in a phantom experiment. The dotted line represents the case where the both T_1 are equal.**

Figure 5. **(a), (b)** M_0 **-weighted and (c), (d)** T_1 **-weighted images through a transverse plane (slice 2) of immature-green cherry tomato.**

Figure 6. **Quantitative M_0, T_1, $\frac{\Delta M_0}{M_0}$ and $\frac{\Delta T_1}{T_1}$ maps through a transverse plane (slice 2) of immature-green cherry tomato. At 1 *h* (a, b, c, d, e and f) and 112 *h* (g, h, i, j, h and l) of dynamic CA uptake. The black pixels (Not a Number) represent areas excluded from the calculation because the error exceeded a 15 $\%$ acceptance criteria.**

Figure 7. **Images segmentation. The red pixels represent the columella and its surrounding tissues. Yellow pixels reflect the seed envelopes and blue pixels are those of other tissues.**

Figure 8. **CA concentration map overlayed over a grayscale anatomical image.**

Figure 9. **The dynamic CA concentration for the columella (× : slice 1, ○ : slice 2, □ : slice 3) with corresponding compartmental models (solid lines).**

Figure 10. **Growth curve. The total volume was determined from all slices by an extrapolation to a spherical volume.**

Figure 11. T_1 **changes in the seed envelopes (○ : slice 2, □ : slice 3, △ : slice 4, ＋ : control tomato). Inset : corresponding** M_0.

Figure 12. **The dynamic CA concentration for the seed envelopes (○ : slice 2, □ : slice 3, △ : slice 4) with corresponding linear regressions (solid lines).**

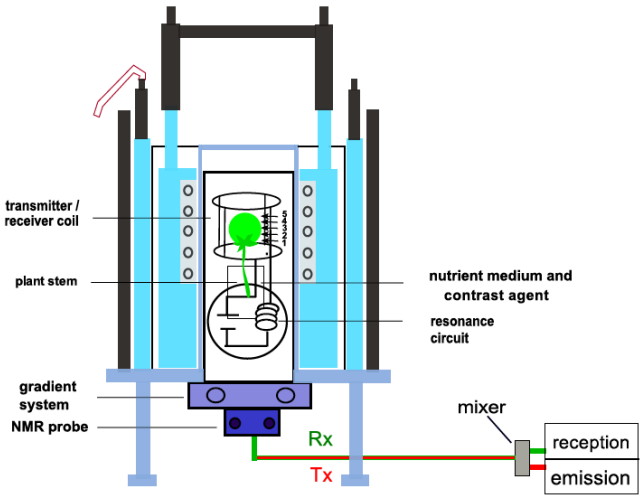

Fig. 1

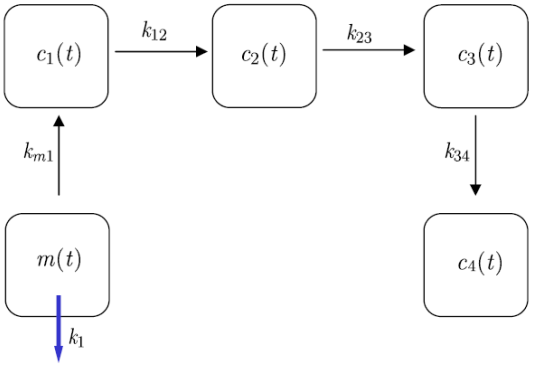

Fig. 2

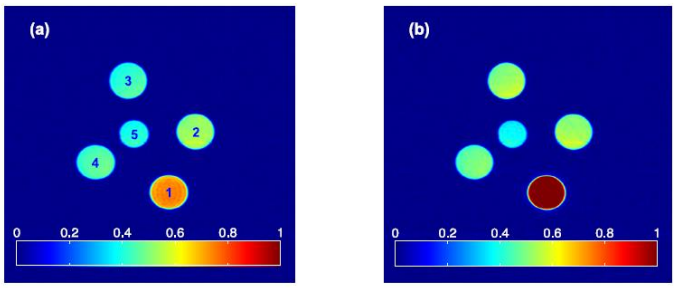

Fig. 3

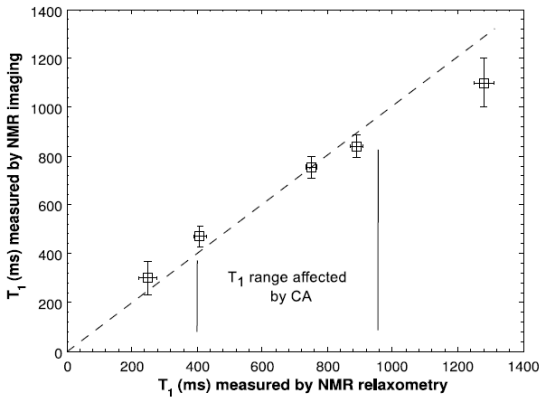

Fig. 4

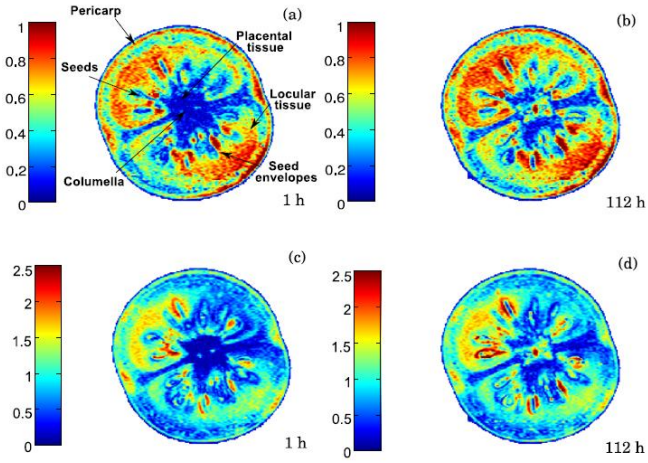

Fig. 5

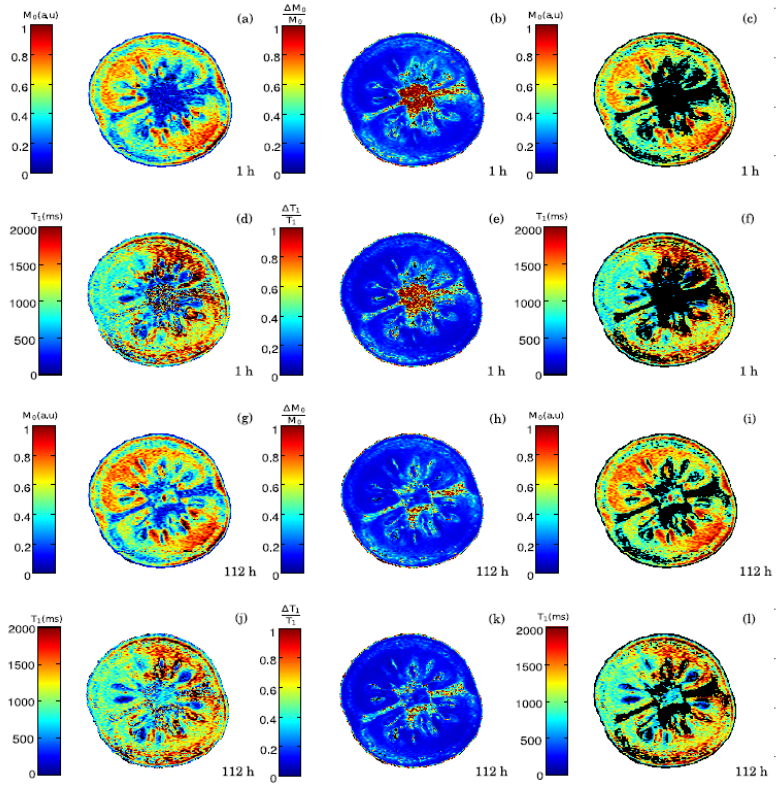

Fig. 6

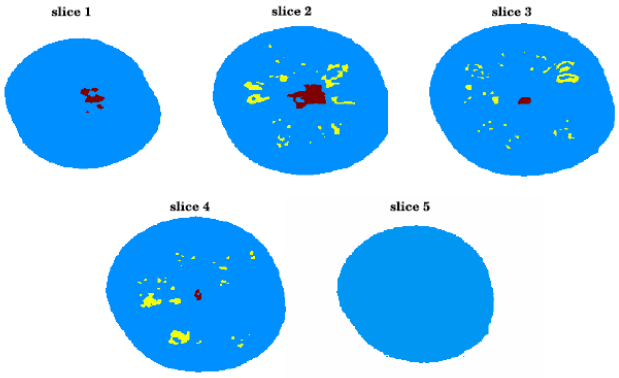

Fig. 7

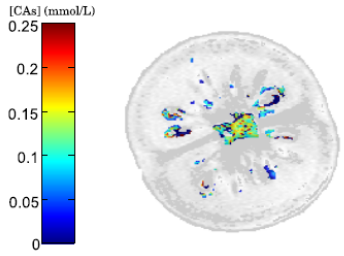

Fig. 8

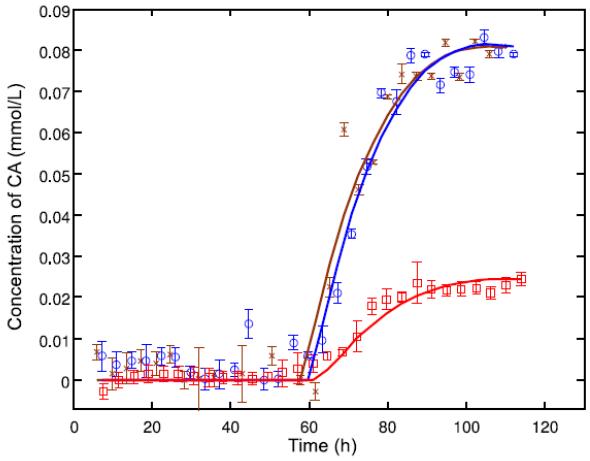

Fig. 9

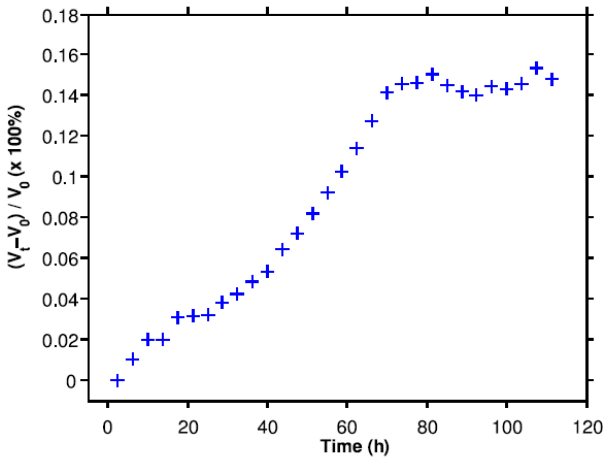

Fig. 10

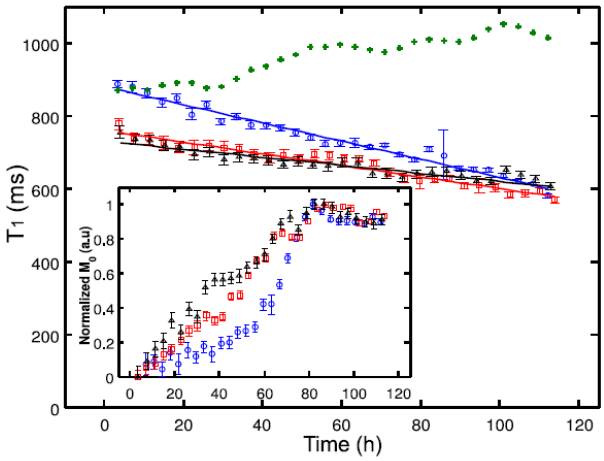

Fig. 11

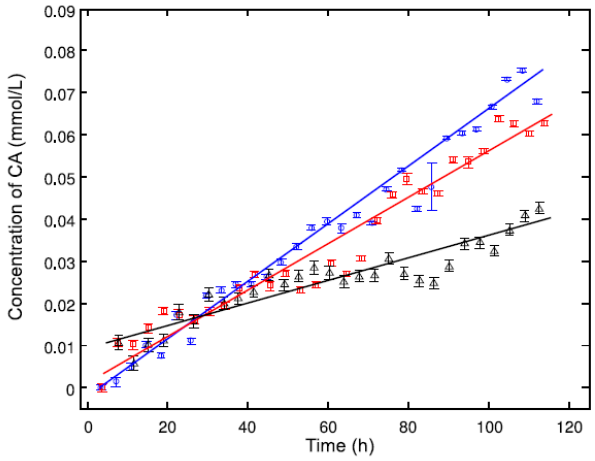

Fig. 12